ACS Energy Letters

http://pubs.acs.org/journal/aelccp

CoV_2O_6–V_2O_5 Coupled with Porous N-Doped Reduced Graphene Oxide Composite as a Highly Efficient Electrocatalyst for Oxygen Evolution

Feng-Cui Shen,[†,‡,§] Yu Wang,[†] Yu-Jia Tang,[†] Shun-Li Li,[†] Yi-Rong Wang,[†] Long-Zhang Dong,[†] Ya-Fei Li,[*,†] Yan Xu,[§] and Ya-Qian Lan[*,†]

[†]Jiangsu Key Laboratory of Biofunctional Materials, School of Chemistry and Materials Science, Nanjing Normal University, Nanjing 210023, PR China

[‡]Department of Biological and Chemical Engineering, Anhui Polytechnic University, Wuhu 241000, PR China

[§]College of Chemistry and Chemical Engineering, State Key Laboratory of Materials-Oriented Chemical Engineering, Nanjing Tech University, Nanjing 210009, PR China

Supporting Information

ABSTRACT: Electrocatalysts with high intrinsic activity for the oxygen evolution reaction (OER) are greatly desired for sustainable oxygen-based electrochemical energy conversion. In this work, the bimetallic oxide composite consisting of CoV_2O_6 and V_2O_5 anchoring on nitrogen-doped reduced graphene oxide (CoV_2O_6–V_2O_5/NRGO-1) was synthesized directly by carbonization of the polyoxometalates, ethylenediamine, and graphene oxide precursors. CoV_2O_6–V_2O_5/NRGO-1 used as an electrocatalyst exhibits an ultralow overpotential of 239 mV vs RHE at the current density of 10 mA cm^{-2} and excellent stability in 1 M KOH. Surprisingly, it has high intrinsic activity with the turnover frequency of 1.80 s^{-1} at the overpotential of 300 mV, which is the highest among the electrocatalysts reported to date. Theoretical calculation proves that the outstanding electrocatalytic performance is attributed to synergistic effects, in which CoV_2O_6 acts as active sites while the hydrogen bond between V_2O_5 and intermediate HOO* of the OER greatly decreases the composite adsorption energy, thus reducing the overpotential. Most importantly, the results demonstrate for the first time that intermolecular hydrogen bonding plays a key role in improving electrocatalytic properties for the OER, which reveals a new method of designing novel OER electrocatalysts.

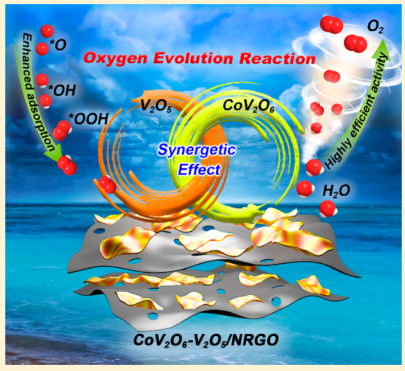

A large amount of energy consumption and urgent need for environmental protection have triggered intense research interest in promising technologies for meeting clean energy requirements and energy conversion efficiency.[1,2] Oxygen evolution reaction (OER) as the key obstacle of splitting water and rechargeable metal–air batteries has stimulated especially substantial efforts.[2−4] OER is a four-electron process involving *OH, *O, and *OOH intermediate multistep proton-coupled electron transfer on the catalysts' surfaces with high overpotential and sluggish kinetics.[5−7] Many efforts have been devoted to exploring the promising non-noble-metal oxides,[8,9] sulfides,[10−12] hydroxides,[7,13,14] phosphides,[15,16] borides,[17] and nitrides[5,18] for OER. However, most of them require relatively higher overpotential[9,19,20] or have sluggish dynamics.[10,17,21]

Comparatively, bimetallic oxide OER catalysts have attracted more attention, because their OER performance precedes that of the corresponding single-metal oxides, which is due to the multimetal oxide modulating the electronic structure and energetics of OER intermediates.[22] Among the bimetallic oxides catalysts, cobalt-based electrocatalysts have been researched as promising OER candidates owing to their excellent charge transport properties.[23,24] Many transition-metal elements such as Ni,[25,26] Fe,[26,27] Mo,[28] Mn,[29] Zn,[30] etc. were incorporated into cobalt-based material to form bimetallic oxide catalysts for water oxidation. In addition, vanadium is an important and earth-abundant element among the transition metals. However, there is only one report using vanadium and cobalt-based bimetallic oxides as an electrocatalyst for OER with the deficiency of relatively high overpotential.[31] To date, vanadium-based double

Received: March 15, 2017
Accepted: May 1, 2017
Published: May 1, 2017

DOI: 10.1021/acsenergylett.7b00229
ACS Energy Lett. 2017, 2, 1327−1333

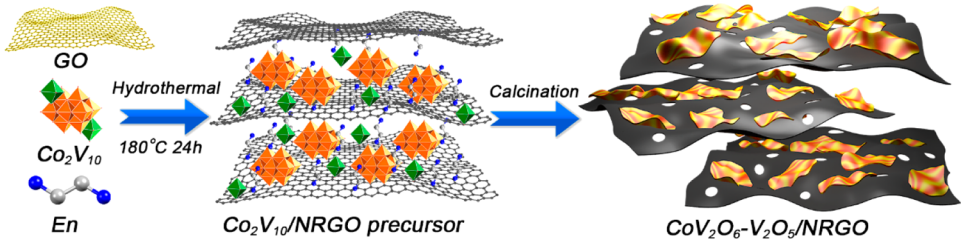

Figure 1. Schematic illustration of the synthetic process of CoV_2O_6–V_2O_5/NRGO-1 composite.

hydroxides have been applied to OER with excellent performance,[13,32] giving us reason to speculate that the vanadium oxide compounds in the highest oxidation state may have good performance for OER because of its active coordination. However, the bimetallic system has raised troublesome questions regarding complicated composition and disorder structures, which might be avoided by many difficult procedures, thus retarding the development of new OER catalysts. As a consequence, the development of a simple method to prepare precursors with stable and uniform structure for use as a perfect platform to gain bimetallic oxide catalysts is a challenge for electrochemistry.

Polyoxovanadates (POVs),[33] as a subfamily of polyoxometalates (POMs), have precise architectures that guarantee the further synthesis of the target compound with quantitative metal atomic ratio. Moreover, polyoxovanadates consisting of different metal atoms have no need to introduce new material source, which greatly avoids the complexity of the system. Therefore, POVs are promising catalyst precursors to explore. In addition, better conductivity and larger specific surface area are indispensable for catalytic activity.[28] Graphene oxide or reduced graphene oxide layers doped with nitrogen can significantly increase the active sites[34] and have been widely employed in electrochemistry catalysts to promote electron transport and larger specific surface area.[35]

In light of these ideas, we first rationally designed a facile, one-pot hydrothermal method integrating polyoxovanadate, ethylenediamine (EN), and graphene oxide (GO) for the model precursor. POVs were chosen to synthesize bimetallic oxides. Ethylenediamine acted as the nitrogen source and reductive agent for GO, while RGO sheets served as a conductive base. With the effect of the flexible structure of EN, it is convenient for the amino hydrogen bond to selectively react with the epoxide groups of GO and construct a three-dimensional (3D) interconnected cross-linking system.[36] Then POMs are easily accessible to the 3D system (Figure 1) with uniform distribution. After carbonization, two-dimensional (2D) porous composites structures consisting of cobalt–vanadium oxides were obtained by EN decomposition causing the expansion of graphene layers. Surprisingly, the composite has a staggering performance for the OER with a high turnover frequency (TOF) of 1.80 s^{-1}, small Tafel slope of 49.7 mV dec^{-1}, and ultralow overpotential of 239 mV at the current density of 10 mA cm^{-2} (η_{10}). Furthermore, it has excellent stability and durability in alkaline electrolyte. In addition, this Letter is the first to use theoretical research to prove that the compound CoV_2O_6–V_2O_5 is an efficient OER electrocatalyst profiting from the synergistic effects, in which the CoV_2O_6 active function can be reinforced by the hydrogen bonds formed by the action of oxygen atoms in V_2O_5 and intermediate *OOH of the OER.

The synthesis of hybrid CoV_2O_6–V_2O_5/NRGO-1 is schematically depicted in Figure 1. We prepared the precursor using a simple hydrothermal method by mixing $[Co(H_2O)_6]_2V_{10}O_{28}\cdot 6H_2O$ (Co_2V_{10}) (Figure S1), EN, and GO (denoted as Co_2V_{10}/RGO). Upon carbonizing at 400 °C for 1 h in air at a heating rate of 5 °C min^{-1}, the obtained sample will undergo the formation of metal oxide V_2O_5 and CoV_2O_6 from Co_2V_{10}. Meanwhile, decomposition of EN and graphitization of GO investigated by Raman analysis (Figure S2) cause the GO sheets to expand or swell to form porous structures. Therefore, the composite was finally obtained with CoV_2O_6 and V_2O_5 anchoring on N-doped porous reduced graphene oxide layers (termed CoV_2O_6–V_2O_5/NRGO-1). Similarly, CoV_2O_6/NRGO was synthesized using the β-CoV_2O_6 instead of Co_2V_{10} without carbonization, while CoV_2O_6/NRGO-1 was synthesized with carbonization. In controlled experiments, the effects of graphene loadings on the OER performance were investigated. CoV_2O_6–V_2O_5/NRGO with different GO concentrations (3 and 7 mg mL^{-1}) were prepared and are denoted as CoV_2O_6–V_2O_5/NRGO-2 and -3, respectively. We also prepared other CoV_2O_6–V_2O_5/NRGO-1 related composites by altering the ratio of GO and EN, denoted as CoV_2O_6–V_2O_5/NC (without GO) and CoV_2O_6–V_2O_5/RGO (without EN); in addition, CoV_2O_6–V_2O_5 was obtained by carbonizing Co_2V_{10}.

The structures of as-synthesized samples were investigated by poweder X-ray diffraction (PXRD). PXRD of related composites are shown in Figures 2a and S3. Their diffraction peaks in Figure 3a indicate that all the composites contain oxides of β-CoV_2O_6 and V_2O_5 corresponding to JCPDS No. 51-130 and 1-359. Interestingly, the phase state of CoV_2O_6 in CoV_2O_6/NRGO-1 changed from JCPDS 51-130 β-CoV_2O_6 to 38-90a-CoV_2O_6 after the carbonization of CoV_2O_6/NRGO (Figure S3b). Scanning electron microscopy (SEM) images of precursor Co_2V_{10}/NRGO indicate that 3D N-doped reduced graphene oxide layers (NRGO) as the conductive substrates ensure the uniform distribution of Co_2V_{10} (Figure 2b). SEM images of the CoV_2O_6–V_2O_5/NRGO-1 in Figures 2c and S4a show porous structures with flakelike morphology due to the existence of NRGO avoiding the accumulation of V_2O_5 and CoV_2O_6. Its transmission electron microscopy (TEM) image is consistent with the SEM image with a large number of slices of V_2O_5 and CoV_2O_6 homogeneously distributed on porous NRGO (Figures 2d and S4b). However, the morphological structures of CoV_2O_6–V_2O_5/NC were different in Figure S5a,b: components of CoV_2O_6 and V_2O_5 easily piled up together under the influence of the van der Waals force. Similarly, CoV_2O_6, V_2O_5, and RGO films of CoV_2O_6–V_2O_5/RGO tend to accumulate owing to the lack of EN's support of the RGO (Figure S6a,b). In addition, SEM and TEM images of CoV_2O_6/NRGO can be seen in Figure S7a,b. They show similar morphologies, with CoV_2O_6 nanoparticles anchoring uniformly on NRGO.

A high-resolution TEM (HRTEM) image of CoV_2O_6–V_2O_5/NRGO-1 is shown in Figure 2e with clear lattice fringe spacing of

DOI: 10.1021/acsenergylett.7b00229
ACS Energy Lett. 2017, 2, 1327−1333

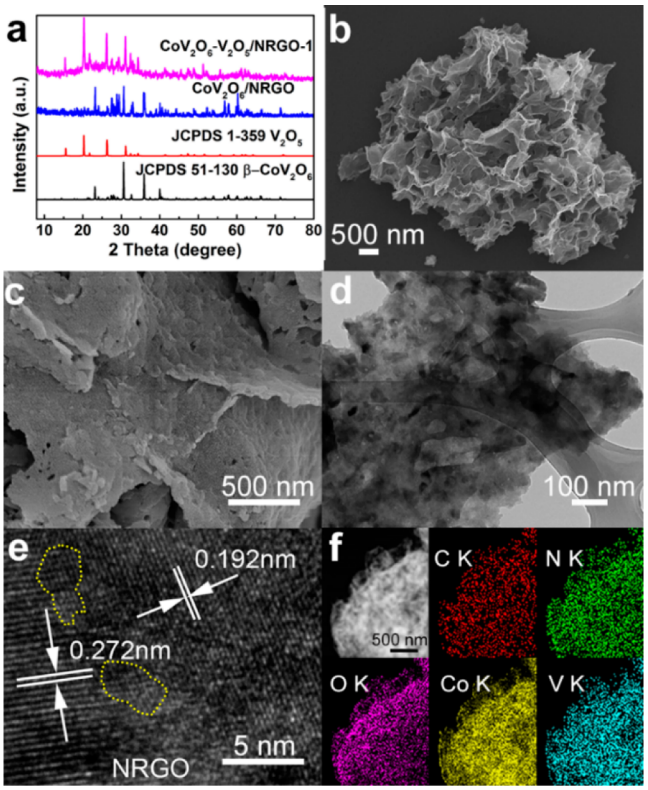

Figure 2. Characterization of the Co_2V_{10}/NRGO and CoV_2O_6–V_2O_5/NRGO-1 composites. (a) XRD patterns of as-prepared samples of CoV_2O_6–V_2O_5/NRGO-1 and CoV_2O_6/NRGO-1. (b) SEM images of Co_2V_{10}/NRGO. (c) SEM, (d) TEM, and (e) HRTEM images of CoV_2O_6–V_2O_5/NRGO-1. (f) EDX elemental mapping of C, N, O, V, and Co of CoV_2O_6–V_2O_5/NRGO.

0.272 nm corresponding to the (111) planes of CoV_2O_6[37] and 0.192 nm corresponding to the ($\bar{1}$14) planes of V_2O_5.[38] It can be clearly seen that the area within the yellow dotted line is the intersection of two lattices fringes of CoV_2O_6 and V_2O_5. We can also see that the lattice fringes space of 0.272 nm of CoV_2O_6/NRGO is consistent with the (111) planes of CoV_2O_6[37] (Figure S7c). The crystallization degree is relatively weak because of the absence of carbonization. Furthermore, the corresponding element mapping analyses of CoV_2O_6–V_2O_5/NRGO-1 (Figure 2f) indicate the homogeneous distributions of element C, N, O, Co, and V in the whole system, which are consistent with its SEM and TEM images. Mappings for CoV_2O_6–V_2O_5/NC and CoV_2O_6/NRGO are shown in Figures S5c and S7d; C, N, O, Co and V elements can be detected uniformly. Mapping for CoV_2O_6–V_2O_5/RGO shows the uniform distribution of C, O, Co, and V elements (Figure S6c). All these samples were also tested by energy dispersive X-ray spectrometry (EDX) (Figure S8).

The water oxidation activities of CoV_2O_6–V_2O_5/NRGO-1 were investigated in N_2-saturated 1 M KOH on glassy carbon electrode (experimental details are in the Supporting Information). For comparison, the grinding mixture of CoV_2O_6–V_2O_5 and acetylene black (CoV_2O_6–V_2O_5-AB), CoV_2O_6/NRGO, and the commercial IrO_2 catalyst were also investigated. All potentials were calibrated to the reversible hydrogen electrode (RHE). As shown in Figure 3a,b, CoV_2O_6/NRGO exhibits a relatively good performance for OER with the overpotential of 379 mV at η_{10}, which is close to that of IrO_2 (337 mV) while the composite CoV_2O_6/NRGO-1 displays relative poor performance for OER in Figure S9, which may be attributed to the crystalline phase change of CoV_2O_6. Interestingly, electrocatalytic activity of CoV_2O_6/NRGO can be dramatically further enhanced by adding V_2O_5, while CoV_2O_6–V_2O_5/NRGO-1 demands only the overpotential of 239 mV at η_{10}. Subsequently, the performance of CoV_2O_6–V_2O_5-AB composite for OER was measured; it demanded the overpotential of 359 mV at η_{10}, which gives full insight into the importance of conductive substrate with nitrogen addition.

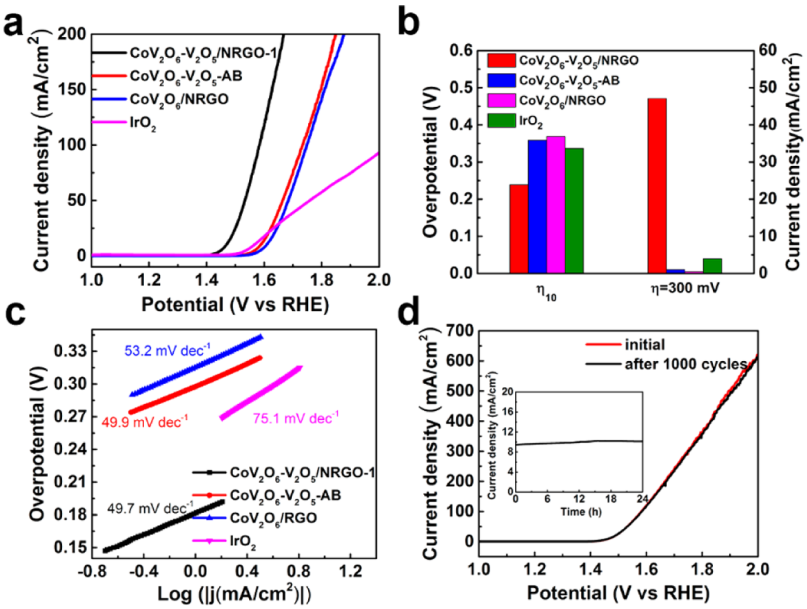

Figure 3. Oxygen evolution performances of electrocatalysts. (a) Polarization curves, (b) comparison of catalysts' overpotential at the current density of 10 mA cm^{-2} (η_{10}), corresponding current density at the overpotential of 300 mV, and (c) corresponding Tafel plots. (d) Initial polarization curves of CoV_2O_6–V_2O_5/NRGO-1 and after 1000 CV cycles. Inset: time-dependent current density curve of CoV_2O_6–V_2O_5/NRGO-1 under the potential of 239 mV for 24 h.

DOI: 10.1021/acsenergylett.7b00229
ACS Energy Lett. 2017, 2, 1327−1333

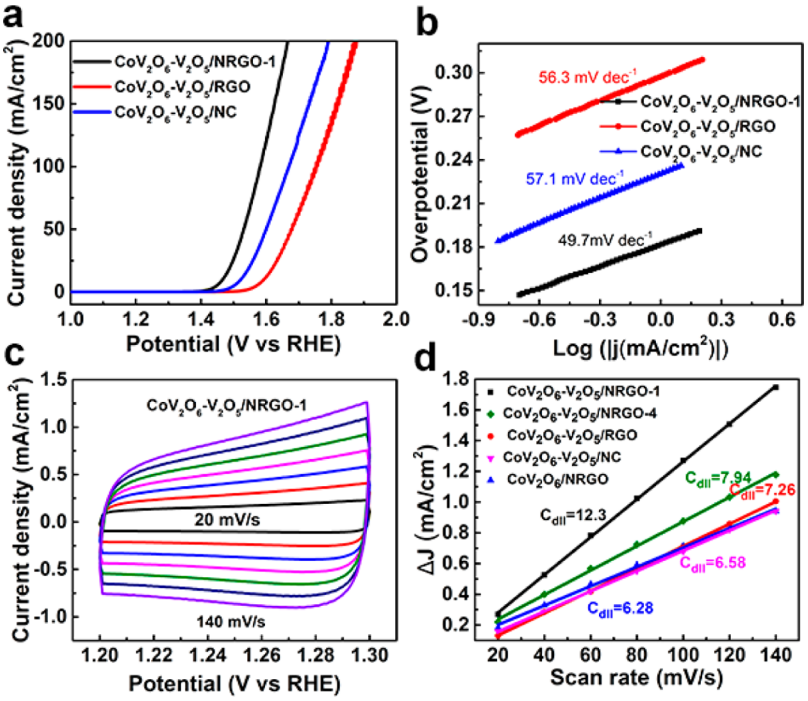

Figure 4. Comparison of the oxygen evolution performance of electrocatalysts. (a) Polarization curves and (b) corresponding Tafel plots. (c) CV curves of CoV_2O_6–V_2O_5/NRGO-1 with different rates from 20 to 140 mV s^{-1}. (d) ΔJ of catalysts plotted against scan rate at the potential of 1.25 V vs RHE. The slopes were used to denote the ECSA.

In addition, the current density of different catalysts was compared at the overpotential of 300 mV (Figure 3b). CoV_2O_6–V_2O_5/NRGO-1 achieved the highest current density of 47.08 mA/cm^{-2}, compared to that of CoV_2O_6–V_2O_5-AB (1.02 mA cm^{-2}), CoV_2O_6/NRGO (0.45 mA cm^{-2}), and IrO_2 (3.95 mA cm^{-2}), which indicates the high oxygen production of CoV_2O_6–V_2O_5/NRGO-1. Such excellent OER activity with ultralow overpotential is superior to most non-noble-metal OER catalysts that have been reported (Table S1).

The Tafel plot is an inherent method to measure the catalytic kinetics for the comparative catalysts by fitting the Tafel equation ($\eta = b \log j + a$, where η is the overpotential, j the current density, and b the Tafel slope). Remarkably, the Tafel slope for CoV_2O_6–V_2O_5/NRGO-1 (49.7 mV dec^{-1}) is lower than that of CoV_2O_6–V_2O_5-AB (49.9 mV dec^{-1}), CoV_2O_6/NRGO (53.2 mV dec^{-1}), and most of the reported OER catalysts. Such a low Tafel slope indicates the faster reaction kinetics, which is probably due to the efficient charge transport and large contact surface in the catalytic process. The long-term stability and durability of electrocatalysts are significant criteria for the application. Long-term stability for CoV_2O_6–V_2O_5/NRGO-1 and CoV_2O_6/NRGO were studied with continuous cyclic voltammetry (CV) cycling between 1.3 and 1.5 V vs RHE at the scan rate of 100 mV s^{-1} in Figures 3d and S10a. As shown, their polarization curves are almost overlapping before and after 1000 cycles, demonstrating their high stability during the catalytic process. In addition, the durability of CoV_2O_6–V_2O_5/NRGO-1 and CoV_2O_6/NRGO was evaluated (Figures 3d and S10b) by chronoamperometry operation at the overpotential of 239 and 379 mV corresponding to the current density of 10 mA/cm^2 with a scan rate of 100 mV s^{-1}. Obviously, there are negligible changes in the current density, which confirmed their excellent durability.

On the basis of the excellent performance of CoV_2O_6–V_2O_5/NRGO-1, different GO loadings effects on the electrocatalytic activity of CoV_2O_6–V_2O_5/NRGO-2 and CoV_2O_6–V_2O_5/NRGO-3 were investigated. As seen from Figure S11a, they showed relatively poor OER performance requiring overpotential of 265 and 249 mV at η_{10} and relative large Tafel plots of 60 and 53.2 mV dec^{-1} (Figure S11b). Catalysts CoV_2O_6–V_2O_5/NRGO-2 and -3 exhibit poor OER performance, which can be attributed to the low concentration of GO loading with poor conductivity and low proton and electron-transfer efficiency. In contrast, high concentration loading may result in the stacking of GO and affect the distribution of the active sites.

To evaluate the impact of different metal ratios, CoV_2O_6–V_2O_5/NRGO-4 was prepared by a similar approach except that Co_2V_{10} was replaced by polyoxovanadate $[Co_3V_{18}O_{42}(H_2O)_{12}(SO_4)]_{24}H_2O$ (Co_3V_{18}) (Figure S12a,b). CoV_2O_6–V_2O_5/NRGO-4 ($n_{CoV_2O_6}$:$n_{V_2O_5}$ = 1:2) (Figure S12c) has the same component with CoV_2O_6–V_2O_5/NRGO-1 ($n_{CoV_2O_6}$:$n_{V_2O_5}$ = 2:3) but has different proportions of Co and V atoms. It shows a relatively high catalytic activity requiring the overpotential of 267 mV at η_{10} with a Tafel plot of 55.5 mV dec^{-1} (Figure S11a,b),which is inferior to CoV_2O_6–V_2O_5/NRGO-1. The higher the ratio of cobalt the composite has, the better the performance it exhibits. Thus, we can confirm the key role of CoV_2O_6 in the hybrid for the OER. The catalytic performance of CoV_2O_6–V_2O_5/NRGO-4 is superior to that of CoV_2O_6, which also reveals the crucial role of the synergistic effect between CoV_2O_6 and V_2O_5.

We also sought to control of precursor composition to evaluate the catalytic activity of the corresponding composite for OER. The electrocatalytic activity and Tafel plot of CoV_2O_6–V_2O_5/NC and CoV_2O_6–V_2O_5/RGO were evaluated in Figure 4ab. Both of them showed relatively low electrocatalytic activity demanding the overpotential of 295 and 366 mV at η_{10}, respectively (Figure 4a), and the Tafel slopes of 57.1 and 56.3 mV dec^{-1} (Figure 4b), which fully proved the

DOI: 10.1021/acsenergylett.7b00229
ACS Energy Lett. 2017, 2, 1327−1333

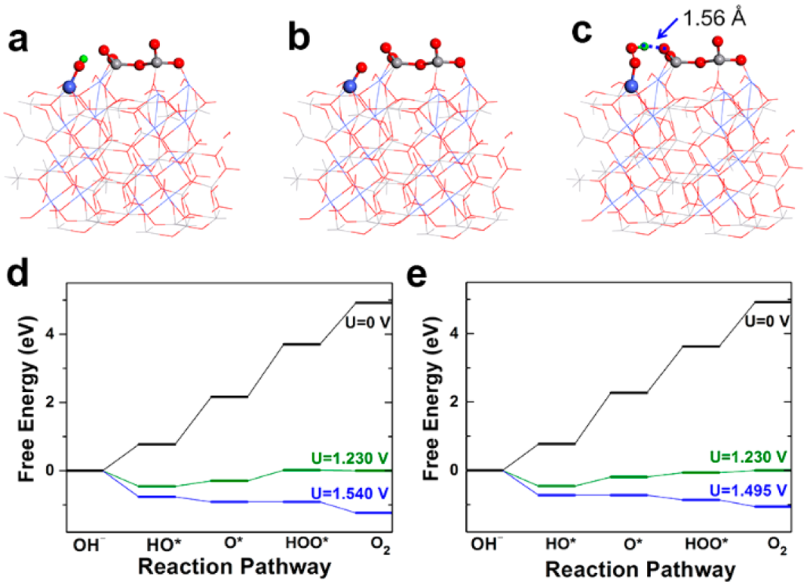

Figure 5. DFT-calculated OER activities. Views of geometric structure of (a) HO*, (b) O*, and (c) HOO* on the active interface of CoV_2O_6–V_2O_5/NRGO-1. HO*, O*, and HOO* are adsorbed intermediates. The blue, gray, red, and green balls represent Co, V, O, and H atoms, respectively. The blue line denotes hydrogen bond. Free-energy profile for the OER pathway on (d) the active regions of CoV_2O_6/NRGO and (e) the active interface of CoV_2O_6–V_2O_5/NRGO-1 at the zero potential (black), the equilibrium potential (green), and the limiting potential (blue).

importance of the conductivity of RGO and the heteroatom nitrogen function.

To provide further insight into the reasons for the highly catalytic activity of OER, the electrochemically active surface areas (ECSA) of the studied catalysts were evaluated by CV at various scan rates in the non-Faradaic region to measure the electrochemical double-layer capacitance (EDLC, C_{dll}) (Figures 4c and S13). Among the catalysts (Figure 4d), the bigger C_{dll} values we get, the larger electrochemically active surface contacting electrolyte benefits for the OER catalytic activity. The electrochemically active surface of CoV_2O_6–V_2O_5/NRGO-1 is nearly twice that of CoV_2O_6/NRGO, making the active sites convenient to contact the electrolyte and release oxygen, which fully proves that the cooperation between CoV_2O_6 and V_2O_5 dramatically improves the catalytic property. Furthermore, the corresponding catalysts' Brunauer–Emmett–Teller (BET) surface areas were investigated by N_2 adsorption isotherms (Figure S14a). Notably, CoV_2O_6–V_2O_5/NRGO-1 has a slightly larger specific surface area that contributes to the increase of the electrochemically active surface and thus improves its electrochemical activity. The diameter of the pores was calculated by Barrett–Joyner–Halenda (BJH) method indicating the mesopores of around 4 nm (Figure S14b). All of the above factors contribute to the high catalytic activity of CoV_2O_6–V_2O_5/RGO-1. The specific catalytic mechanism will be explained by the theoretical calculation in the following sections.

The aforementioned experimental results indicate that CoV_2O_6/NRGO has a good catalytic performance for OER, which can be further improved by the coupling of V_2O_5. However, the underlying mechanism for the appealing synergistic effect is still unclear. To this end, the spin-polarized density-functional theory (DFT) computations were performed to gain some fundamental insight into the catalytic performance of those complexes toward OER. The possible OER processes are listed in eqs S1–S4. First, we investigated the origin of overpotential for OER over CoV_2O_6/NRGO by calculating the free-energy change for the electrochemical steps (ΔG_{1-4}) based on the computational hydrogen electrode (CHE) model.[39] The energetically favorable low-index CoV_2O_6 (010) plane was chosen as the active regions for CoV_2O_6/NRGO (see Note S1 for details). As shown in Figure 5a, all reaction steps are uphill at zero potential, and the middle two steps, especially ΔG_3, are still uphill at the equilibrium potential (U = 1.230 V). Until the potential is increased to 1.540 V, all reactions become exothermic. Therefore, OER over CoV_2O_6/NRGO is limited by the conversion of O* to OOH*, of which the theoretical overpotential (η_{the}) is 310 mV. The analysis also reveals that this overpotential originated from its rather weak HOO* binding and strong O* adsorption compared with an ideal OER catalyst, because ΔG_3 is determined by the difference between the adsorption free energy of HOO* (ΔG_{HOO*}) and O* (ΔG_{O*}).

Then an intriguing question arises: does CoV_2O_6–V_2O_5/NRGO possess more energetically favorable ΔG_{HOO*} and ΔG_{O*} than CoV_2O_6/NRGO because CoV_2O_6–V_2O_5/NRGO was detected experimentally to have a lower overpotential? In this regard, we further explored the adsorption of those intermediates on the active interface of CoV_2O_6–V_2O_5/NRGO (Figure S18). After full atomic relaxation, a strong hydrogen bonding between HOO* species and the active interface of this composite is found, which intrinsically enhances the binding strength of HOO*. Moreover, the adsorption of O* is slightly weak after the coupling of V_2O_5, and consequently, the ΔG_3 is turned into a favorable value of 1.356 eV. This result is very inspiring because it is known that the binding energy of HOO* and O* are linearly correlated with a positive slope.[40,41] However, this linear relationship is absent in CoV_2O_6–V_2O_5 because of the weak interaction of hydrogen bonding. The free-energy changes along the full OER process over the active interface of CoV_2O_6–V_2O_5/NRGO are shown in Figure 5e. As expected, electrochemical steps require a potential of only 1.495 V to become exothermic. Interestingly, the OER on CoV_2O_6–V_2O_5/NRGO is not limited by the third step but determinded by the

DOI: 10.1021/acsenergylett.7b00229
ACS Energy Lett. 2017, 2, 1327–1333

second step, and its η_{the} reduced to 265 mV, which is in good agreement with our measurements (239 mV at 10 mA cm^{-2}). Note here that the beneficial role of NRGO supports is not captured by this theoretical computation, whereas RGO might enhance the catalytic activity via the significant electrical conductivity improvement.

We further applied the turnover frequency (TOF) to evaluate CoV_2O_6–V_2O_5/NRGO-1 intrinsic activity, which was calculated based on only surface-active sites on the working electrodes.[42,43] Theoretical calculation research has verified that CoV_2O_6 acts as active sites in the CoV_2O_6–V_2O_5/NRGO composite, while V_2O_5 acts as the adsorbent of intermediate HOO*. Therefore, the TOF of the composite is calculated based on only the amount of CoV_2O_6 whose quality can be calculated from the ratio of the element cobalt in the hybrid obtained from the XPS data (Figure S15) in the composite of CoV_2O_6–V_2O_5. We assume that all cobalt ions in the hybrid are catalytically active; some active sites are electrochemically inaccessible, though. Surprisingly, CoV_2O_6–V_2O_5/NRGO-1 achieved the highest TOF of 1.80 s^{-1} among all the reported data at the overpotential of 300 mV (Table S1). The kinetics of electrode interface reactions were also studied by the electrochemical impedance spectroscopy technique for all the relevant samples (Figure S16). Apparently, CoV_2O_6–V_2O_5/NRGO-1 exhibits a much smaller semicircle than that of other catalysts, suggesting the lower impedance and the higher efficient charge transfer between the interfaces, which can be due to the porous structure shortening ion diffusion distance and the good conductivity of NRGO. We obtained all the polarization curves in Figure S17 with *iR*-compensation based on the ohmic drop.[44] In addition, overpotentials of the corresponding catalysts and the current density at η = 300 mV are listed in Table S2.

In summary, we successfully synthesized a catalyst CoV_2O_6–V_2O_5/NRGO-1 through a simple and convenient method. The as-synthesized composite is one of the best catalysts for OER with ultralow overpotential, low Tafel plot, and the highest TOF in 1 M KOH, which is even comparable with the state-of-the-art electrocatalysts. The excellent performance is mainly attributed to the composite "killing two birds with one stone". The hydrogen bond between V_2O_5 and intermediate HOO* of OER decreases its adsorption energy, which is coupled with the activation of CoV_2O_6 and thus greatly reduces the overpotential. In addition, theoretical calculation proved for the first time that the hydrogen bond plays a key role in the water oxidation. In addition, the catalyst also exhibits good stability and long-time durability in alkaline solutions. All the results demonstrate that it is indeed an excellent electrocatalyst combining high intrinsic catalytic activity and stability for water oxidation. In addition, the bimetallic oxide composite with precise metal atomic ratio resulting from the controlled synthesis of precursors provides a versatile platform to design efficient and novel electrocatalysts for energy conversion applications.

■ ASSOCIATED CONTENT

Supporting Information

The Supporting Information is available free of charge on the ACS Publications website at DOI: 10.1021/acsenergylett.7b00229.

Detailed information regarding the experimental methods, computational details, related electrocatalyst characterization, and electrochemical performance (PDF)

■ AUTHOR INFORMATION

Corresponding Authors

*E-mail: yqlan@njnu.edu.cn.
*E-mail: liyafei@njnu.edu.cn.

ORCID

Long-Zhang Dong: 0000-0002-9276-5101
Yan Xu: 0000-0001-6059-075X
Ya-Qian Lan: 0000-0002-2140-7980

Notes

The authors declare no competing financial interest.

■ ACKNOWLEDGMENTS

This work was financially supported by NSFC (21622104, 21371099, and 21471080), the NSF of Jiangsu Province of China (BK20130043 and BK20141445), the Priority Academic Program Development of Jiangsu Higher Education Institutions, the Foundation of Jiangsu Collaborative Innovation Center of Biomedical Functional Materials, and Jiangsu Planned Projects for Postdoctoral Research Funds (1601087C).

■ REFERENCES

(1) Liang, Y.; Li, Y.; Wang, H.; Zhou, J.; Wang, J.; Regier, T.; Dai, H. Co_3O_4 nanocrystals on graphene as a synergistic catalyst for oxygen reduction reaction. *Nat. Mater.* **2011**, *10*, 780–786.

(2) Zhao, Y.; Nakamura, R.; Kamiya, K.; Nakanishi, S.; Hashimoto, K. Nitrogen-doped carbon nanomaterials as non-metal electrocatalysts for water oxidation. *Nat. Commun.* **2013**, *4*, 2390.

(3) Zhang, J.; Zhao, Z.; Xia, Z.; Dai, L. A metal-free bifunctional electrocatalyst for oxygen reduction and oxygen evolution reactions. *Nat. Nanotechnol.* **2015**, *10*, 444–452.

(4) Wang, H.; Lee, H. W.; Deng, Y.; Lu, Z.; Hsu, P. C.; Liu, Y.; Lin, D.; Cui, Y. Bifunctional non-noble metal oxide nanoparticle electrocatalysts through lithium-induced conversion for overall water splitting. *Nat. Commun.* **2015**, *6*, 7261.

(5) Xu, K.; Chen, P.; Li, X.; Tong, Y.; Ding, H.; Wu, X.; Chu, W.; Peng, Z.; Wu, C.; Xie, Y. Metallic nickel nitride nanosheets realizing enhanced electrochemical water oxidation. *J. Am. Chem. Soc.* **2015**, *137*, 4119–4125.

(6) Shan, Z.; Archana, P. S.; Shen, G.; Gupta, A.; Bakker, M. G.; Pan, S. NanoCOT: Low-Cost Nanostructured Electrode Containing Carbon, Oxygen, and Titanium for Efficient Oxygen Evolution Reaction. *J. Am. Chem. Soc.* **2015**, *137*, 11996–12005.

(7) Gao, M.; Sheng, W.; Zhuang, Z.; Fang, Q.; Gu, S.; Jiang, J.; Yan, Y. Efficient water oxidation using nanostructured alpha-nickel-hydroxide as an electrocatalyst. *J. Am. Chem. Soc.* **2014**, *136*, 7077–7084.

(8) Kim, J.; Yin, X.; Tsao, K. C.; Fang, S.; Yang, H. $Ca_2Mn_2O_5$ as oxygen-deficient perovskite electrocatalyst for oxygen evolution reaction. *J. Am. Chem. Soc.* **2014**, *136*, 14646–14649.

(9) Meng, Y.; Song, W.; Huang, H.; Ren, Z.; Chen, S. Y.; Suib, S. L. Structure-property relationship of bifunctional MnO_2 nanostructures: highly efficient, ultra-stable electrochemical water oxidation and oxygen reduction reaction catalysts identified in alkaline media. *J. Am. Chem. Soc.* **2014**, *136*, 11452–11464.

(10) Zhou, W.; Wu, X.-J.; Cao, X.; Huang, X.; Tan, C.; Tian, J.; Liu, H.; Wang, J.; Zhang, H. Ni_3S_2 nanorods/Ni foam composite electrode with low overpotential for electrocatalytic oxygen evolution. *Energy Environ. Sci.* **2013**, *6*, 2921.

(11) Chen, B.; Li, R.; Ma, G.; Gou, X.; Zhu, Y.; Xia, Y. Cobalt sulfide/N,S codoped porous carbon core-shell nanocomposites as superior bifunctional electrocatalysts for oxygen reduction and evolution reactions. *Nanoscale* **2015**, *7*, 20674–20684.

(12) Mabayoje, O.; Shoola, A.; Wygant, B. R.; Mullins, C. B. The Role of Anions in Metal Chalcogenide Oxygen Evolution Catalysis: Electrodeposited Thin Films of Nickel Sulfide as "Pre-catalysts. *ACS Energy Letters* **2016**, *1*, 195–201.

DOI: 10.1021/acsenergylett.7b00229
ACS Energy Lett. 2017, 2, 1327–1333

(13) Fan, K.; Chen, H.; Ji, Y.; Huang, H.; Claesson, P. M.; Daniel, Q.; Philippe, B.; Rensmo, H.; Li, F.; Luo, Y.; et al. Nickel-vanadium monolayer double hydroxide for efficient electrochemical water oxidation. *Nat. Commun.* **2016**, *7*, 11981.

(14) Gong, M.; Li, Y.; Wang, H.; Liang, Y.; Wu, J. Z.; Zhou, J.; Wang, J.; Regier, T.; Wei, F.; Dai, H. An advanced Ni-Fe layered double hydroxide electrocatalyst for water oxidation. *J. Am. Chem. Soc.* **2013**, *135*, 8452−8455.

(15) Masa, J.; Barwe, S.; Andronescu, C.; Sinev, I.; Ruff, A.; Jayaramulu, K.; Elumeeva, K.; Konkena, B.; Roldan Cuenya, B.; Schuhmann, W. Low Overpotential Water Splitting Using Cobalt−Cobalt Phosphide Nanoparticles Supported on Nickel Foam. *ACS Energy Letters* **2016**, *1*, 1192−1198.

(16) Dutta, A.; Samantara, A. K.; Dutta, S. K.; Jena, B. K.; Pradhan, N. Surface-Oxidized Dicobalt Phosphide Nanoneedles as a Nonprecious, Durable, and Efficient OER Catalyst. *ACS Energy Letters* **2016**, *1*, 169−174.

(17) Chen, P.; Xu, K.; Zhou, T.; Tong, Y.; Wu, J.; Cheng, H.; Lu, X.; Ding, H.; Wu, C.; Xie, Y. Strong-Coupled Cobalt Borate Nanosheets/Graphene Hybrid as Electrocatalyst for Water Oxidation Under Both Alkaline and Neutral Conditions. *Angew. Chem., Int. Ed.* **2016**, *55*, 2488−2492.

(18) Jia, X.; Zhao, Y.; Chen, G.; Shang, L.; Shi, R.; Kang, X.; Waterhouse, G. I. N.; Wu, L.-Z.; Tung, C.-H.; Zhang, T. Ni_3FeN Nanoparticles Derived from Ultrathin NiFe-Layered Double Hydroxide Nanosheets: An Efficient Overall Water Splitting Electrocatalyst. *Adv. Energy Mater.* **2016**, *6*, 1502585.

(19) Tahir, M.; Mahmood, N.; Zhang, X.; Mahmood, T.; Butt, F. K.; Aslam, I.; Tanveer, M.; Idrees, F.; Khalid, S.; Shakir, I.; et al. Bifunctional catalysts of Co_3O_4@GCN tubular nanostructured (TNS) hybrids for oxygen and hydrogen evolution reactions. *Nano Res.* **2015**, *8*, 3725−3736.

(20) Ledendecker, M.; Krick Calderon, S.; Papp, C.; Steinruck, H. P.; Antonietti, M.; Shalom, M. The synthesis of nanostructured Ni_5P_4 films and their use as a non-noble bifunctional electrocatalyst for full water splitting. *Angew. Chem., Int. Ed.* **2015**, *54*, 12361−12365.

(21) Zhao, Y.; Sun, B.; Huang, X.; Liu, H.; Su, D.; Sun, K.; Wang, G. Porous graphene wrapped CoO nanoparticles for highly efficient oxygen evolution. *J. Mater. Chem. A* **2015**, *3*, 5402−5408.

(22) Zhang, B.; Zheng, X. L.; Voznyy, O.; Comin, R.; Bajdich, M.; Garcia-Melchor, M.; Han, L. L.; Xu, J. X.; Liu, M.; Zheng, L. R.; et al. Homogeneously dispersed multimetal oxygen-evolving catalysts. *Science* **2016**, *352*, 333−337.

(23) Zhang, X.; Liu, R.; Zang, Y.; Liu, G.; Wang, G.; Zhang, Y.; Zhang, H.; Zhao, H. Co/CoO nanoparticles immobilized on Co-N-doped carbon as trifunctional electrocatalysts for oxygen reduction, oxygen evolution and hydrogen evolution reactions. *Chem. Commun.* **2016**, *52*, 5946−5949.

(24) Wang, J.; Cui, W.; Liu, Q.; Xing, Z.; Asiri, A. M.; Sun, X. Recent Progress in Cobalt-Based Heterogeneous Catalysts for Electrochemical Water Splitting. *Adv. Mater.* **2016**, *28*, 215−230.

(25) Yin, J.; Zhou, P.; An, L.; Huang, L.; Shao, C.; Wang, J.; Liu, H.; Xi, P. Self-supported nanoporous $NiCo_2O_4$ nanowires with cobalt-nickel layered oxide nanosheets for overall water splitting. *Nanoscale* **2016**, *8*, 1390−1400.

(26) Bothra, P.; Pati, S. K. Activity of Water Oxidation on Pure and (Fe, Ni, and Cu)-Substituted Co_3O_4. *ACS Energy Letters* **2016**, *1*, 858−862.

(27) Liu, Y.; Li, J.; Li, F.; Li, W.; Yang, H.; Zhang, X.; Liu, Y.; Ma, J. A facile preparation of $CoFe_2O_4$ nanoparticles on polyaniline-functionalised carbon nanotubes as enhanced catalysts for the oxygen evolution reaction. *J. Mater. Chem. A* **2016**, *4*, 4472−4478.

(28) Li, B. B.; Liang, Y. Q.; Yang, X. J.; Cui, Z. D.; Qiao, S. Z.; Zhu, S. L.; Li, Z. Y.; Yin, K. MoO_2-CoO coupled with a macroporous carbon hybrid electrocatalyst for highly efficient oxygen evolution. *Nanoscale* **2015**, *7*, 16704−16714.

(29) Cao, X.; Yan, W.; Jin, C.; Tian, J.; Ke, K.; Yang, R. Surface modification of $MnCo_2O_4$ with conducting polypyrrole as a highly active bifunctional electrocatalyst for oxygen reduction and oxygen evolution reaction. *Electrochim. Acta* **2015**, *180*, 788−794.

(30) Liu, Z. Q.; Cheng, H.; Li, N.; Ma, T. Y.; Su, Y. Z. $ZnCo_2O_4$ Quantum Dots Anchored on Nitrogen-Doped Carbon Nanotubes as Reversible Oxygen Reduction/Evolution Electrocatalysts. *Adv. Mater.* **2016**, *28*, 3777−3784.

(31) Xiao, M.; Yang, D.; Yan, Y.; Tian, Y.; Zhou, M.; Hao, M.; Cheng, R.; Miao, Y. Nanoplates and Nanospheres of $Co_3(VO_4)_2$ as Noble Metal-free Electrocatalysts for Oxygen Evolution. *Electrochim. Acta* **2015**, *180*, 260−267.

(32) Shi, H.; Liang, H.; Ming, F.; Wang, Z. Efficient Overall Water-Splitting Electrocatalysis Using Lepidocrocite VOOH Hollow Nanospheres. *Angew. Chem., Int. Ed.* **2017**, *56*, 573−577.

(33) Khan, M. I.; Yohannes, E.; Doedens, R. J. $[M_3V_{18}O_{42}(H_2O)_{12}(XO_4)]\cdot 24\ H_2O$ (M = Fe, Co; X = V, S): Metal Oxide Based Framework Materials Composed of Polyoxovanadate Clusters. *Angew. Chem., Int. Ed.* **1999**, *38*, 1292−1294.

(34) Guo, D.; Shibuya, R.; Akiba, C.; Saji, S.; Kondo, T.; Nakamura, J. Active sites of nitrogen-doped carbon materials for oxygen reduction reaction clarified using model catalysts. *Science* **2016**, *351*, 361.

(35) Safizadeh, F.; Ghali, E.; Houlachi, G. Electrocatalysis developments for hydrogen evolution reaction in alkaline solutions − A Review. *Int. J. Hydrogen Energy* **2015**, *40*, 256−274.

(36) Liu, Y.; Liu, S.; Lai, X.; Miao, J.; He, D.; Li, N.; Luo, F.; Shi, Z.; Liu, S. Polyoxometalate-Modified Sponge-Like Graphene Oxide Monolith with High Proton-Conducting Performance. *Adv. Funct. Mater.* **2015**, *25*, 4480−4485.

(37) Ni, S.; Ma, J.; Zhang, J.; Yang, X.; Zhang, L. Electrochemical performance of cobalt vanadium oxide/natural graphite as anode for lithium ion batteries. *J. Power Sources* **2015**, *282*, 65−69.

(38) Sathiya, M.; Prakash, A. S.; Ramesha, K.; Tarascon, J. M.; Shukla, A. K. V_2O_5-Anchored Carbon Nanotubes for Enhanced Electrochemical Energy Storage. *J. Am. Chem. Soc.* **2011**, *133*, 16291−16299.

(39) Norskov, J. K.; Rossmeisl, J.; Logadottir, A.; Lindqvist, L.; Kitchin, J. R.; Bligaard, T.; Jonsson, H. Origin of the overpotential for oxygen reduction at a fuel-cell cathode. *J. Phys. Chem. B* **2004**, *108*, 17886−17892.

(40) Rossmeisl, J.; Logadottir, A.; Nørskov, J. K. Electrolysis of water on (oxidized) metal surfaces. *Chem. Phys.* **2005**, *319*, 178−184.

(41) Man, I. C.; Su, H.-Y.; Calle-Vallejo, F.; Hansen, H. A.; Martínez, J. I.; Inoglu, N. G.; Kitchin, J.; Jaramillo, T. F.; Nørskov, J. K.; Rossmeisl, J. Universality in Oxygen Evolution Electrocatalysis on Oxide Surfaces. *ChemCatChem* **2011**, *3*, 1159−1165.

(42) Zhang, B.; Zheng, X.; Voznyy, O.; Comin, R.; Bajdich, M.; Garcia-Melchor, M.; Han, L.; Xu, J.; Liu, M.; Zheng, L.; et al. Homogeneously dispersed multimetal oxygen-evolving catalysts. *Science* **2016**, *352*, 333−337.

(43) Gong, M.; Li, Y.; Wang, H.; Liang, Y.; Wu, J. Z.; Zhou, J.; Wang, J.; Regier, T.; Wei, F.; Dai, H. An Advanced Ni−Fe Layered Double Hydroxide Electrocatalyst for Water Oxidation. *J. Am. Chem. Soc.* **2013**, *135*, 8452−8455.

(44) Yoon, D.; Seo, B.; Lee, J.; Nam, K. S.; Kim, B.; Park, S.; Baik, H.; Hoon Joo, S.; Lee, K. Facet-controlled hollow Rh_2S_3 hexagonal nanoprisms as highly active and structurally robust catalysts toward hydrogen evolution reaction. *Energy Environ. Sci.* **2016**, *9*, 850−856.

DOI: 10.1021/acsenergylett.7b00229
ACS Energy Lett. 2017, 2, 1327−1333